ASCE

Topology Optimization of Energy-Dissipating Plastic Structures with Shear Modified Gurson–Tvergaard–Needleman Model

Lei Li, A.M.ASCE[1]; and Kapil Khandelwal, A.M.ASCE[2]

Abstract: This paper presents a density-based topology optimization framework for designing energy-dissipating plastic structures. In order to mitigate the material damage during the plastic energy dissipation process, the total material volume in a design is minimized while subjected to a minimum plastic work constraint and a maximum damage constraint. The Gurson–Tvergaard–Needleman (GTN) model with shear damage modifications is adopted to simulate the physics of ductile-damage mechanisms under various stress states. Path-dependent design sensitivities are analytically derived using the adjoint method within the framework of nonlinear finite element analysis. The effectiveness of the proposed framework is demonstrated by a series of numerical examples that shows the proposed framework can successfully limit damage in optimized plastic designs under the prescribed threshold by reconfiguring structural topologies. More notably, compared to the designs obtained with the von Mises plasticity model, damage constrained plastic designs with the GTN model have overall better ductility, higher load carrying capacity, and higher plastic work dissipation before failure initiation. **DOI: 10.1061/(ASCE)ST.1943-541X.0002790.**

Author keywords: Energy-dissipating plastic structures; Topology optimization; Gurson–Tvergaard–Needleman (GTN) model; Plasticity; Adjoint sensitivity analysis.

Introduction

Advancements in additive manufacturing (AM) technologies are fundamentally changing how products and components are designed and manufactured (Gibson et al. 2014). Unlike the traditional formative and subtractive manufacturing, AM builds structures by material deposition layer upon layer, reducing or eliminating the restrictions on geometrical complexity in the design. As a result, more emphasis can be placed into the design phase to further optimize the structural performance by making use of the expanded design freedom enabled by AM. As an advanced design method, topology optimization is ideally suited for structural topology designs in conjunction with AM due to its free-form formulation as compared to traditional sizing and shape optimizations, which can only work with the predefined structural configurations (Bendsøe and Sigmund 2003). Due to this natural synergy between AM and topology optimization (Liu et al. 2018), there is an increasing interest in developing topology optimization methods that can be used for the design of advanced structural systems (Sigmund and Maute 2013).

Topology optimization has experienced many developments since its initiation (Bendsøe and Kikuchi 1988), and various topology optimization methods have been proposed and used in a variety of civil, aerospace, automobile, energy, and medical engineering applications (Deaton and Grandhi 2014). Indeed, topology optimization methods are now well established for designing linear structural systems, and these methods have been applied to many applications in structural engineering, see for instance (Beghini et al. 2015; Changizi and Jalalpour 2017; Galjaard et al. 2015; Jewett and Carstensen 2019; Lee and Tovar 2014; Liang et al. 2002; Mijar et al. 1998; Nabaki et al. 2019; Rahmatalla and Swan 2003; Zhang et al. 2016b; Zuo et al. 2011). As compared to the linear elastic designs, topology optimization methods are not yet well established for inelastic (nonlinear) systems design. In many applications, however, structural systems are designed in the inelastic range where the goal is to dissipate energy via inelastic material behavior, and the objective is to maximize the inelastic energy dissipation while constraining the material damage during the energy dissipation process. An important application is the design of metallic systems where the inelastic material behavior is governed by plasticity in conjunction with damage that is associated with nucleation, growth, and coalescence of microvoids that finally leads to ductile fracture (Anderson 2017; Garrison and Moody 1987). In this case, the objective is to design systems that can dissipate as much energy as possible via plastic work while obviating material failures due to ductile fractures. At present, the design of such systems is mostly based on experience, intuition, and trial-and-error based experiments. However, topology optimization provides an alternative paradigm for designing energy-dissipating structures while controlling the damage due to ductile fracture mechanisms, which is the focus of this paper.

To design energy-dissipating plastic structural systems while constraining the overall damage, high-fidelity models should be used to capture the physics of material damage during the topology optimization process. In metals, material damage under applied loads is due to the multistep processes at microscales associated with the nucleation, growth, and coalescence of microvoids (Benzerga and Leblond 2010; Tvergaard 1989). The damage process starts

[1]Postdoctoral Scholar, Dept. of Structural Engineering, Univ. of California, San Diego, 9500 Gilman Dr., SME-443A, La Jolla, CA 92093. ORCID: https://orcid.org/0000-0002-2688-1243. Email: lel008@eng.ucsd.edu

[2]Associate Professor, Dept. of Civil and Environmental Engineering and Earth Sciences, Univ. of Notre Dame, 156 Fitzpatrick Hall, Notre Dame, IN 46556 (corresponding author). ORCID: https://orcid.org/0000-0002-5748-6019. Email: kapil.khandelwal@nd.edu

Note. This manuscript was submitted on July 26, 2019; approved on May 5, 2020; published online on August 19, 2020. Discussion period open until January 19, 2021; separate discussions must be submitted for individual papers. This paper is part of the ***Journal of Structural Engineering***, © ASCE, ISSN 0733-9445.

when microvoids nucleate in the metal matrix. These microvoids then grow in a plastically deforming matrix under evolving stress states, and in the final stage, the microvoids coalesce, leading to ductile fracture initiation. Due to its high technological and engineering significance, many models have been proposed in the literature to simulate the physics of inelastic damage that leads to ductile fracture in metals (Benzerga and Leblond 2010; Benzerga et al. 2016). Among other models, the micromechanically motivated plasticity model proposed by Gurson (1977) is perhaps the most widely used model to simulate damage in metals due to ductile fracture mechanisms (El-Tawil et al. 2014; Khandelwal and El-Tawil 2007; Kiran and Khandelwal 2014; Qian et al. 2005). Using an upper bound approach, Gurson (1977) proposed a yield criterion and flow rules for rigid plastic materials with microvoids. As compared to the von Mises (J_2) yield criterion, the Gurson yield criterion is pressure dependent, and an internal variable termed void volume fraction was introduced to represent the proportion of microvoids. The Gurson yield criterion was subsequently modified by Tvergaard (1982) and Tvergaard and Needleman (1984) to account for the microvoid interactions and the rapid loss of load carrying capacity at the onset of microvoid coalescence. With these modifications, the Gurson model is then renamed the Gurson–Tvergaard–Needleman (GTN) model and is now commonly used to model failures due to ductile fracture. In more recent enhancements, the GTN model was further extended by Nahshon and Hutchinson (2008) based on the Lode parameter to account for shear failures under low-stress triaxialities. Later on, Nielsen and Tvergaard (2010) introduced an additional stress state dependent factor on the shear damage term to eliminate the influence of the Lode parameter at high-stress triaxialities. With these latest enhancements, the GTN model represents the state-of-the-art model to simulate damage to due ductile fracture mechanisms in metals and is therefore adopted for the topology optimization study in this work.

Designing structural systems to achieve required plastic energy dissipation while simultaneously constraining the material damage is a challenging topic in topology optimization. In recent studies, the authors and coworkers have made some progress in this direction (Alberdi and Khandelwal 2017; Li et al. 2017; Li et al. 2018; Zhang et al. 2016a), where the emphasis was on the incorporation of plasticity models in topology optimization, which in itself is a nontrivial task (Alberdi et al. 2018), while the consideration of inelastic damage was secondary. As a result, only simple and approximate damage models were considered in these studies. To achieve a more realistic design framework for plastic energy dissipation, however, the simulation of energy dissipation together with an accurate description of inelastic material damage is required. To this end, this study makes the first effort to incorporate the micromechanically informed GTN model in a density-based topology optimization framework for the design of inelastic structures, wherein the physics of ductile fracture mechanisms can be appropriately controlled during the topology optimization process. To capture the accurate physics of material failure under high- and low-stress triaxialities, the GTN model with shear failure modifications proposed by Nahshon and Hutchinson (2008) and Nielsen and Tvergaard (2010) is used. A maximum damage constrained topology optimization formulation is considered to limit the damage under the prescribed values. An adjoint method is used to obtain consistent analytical design sensitivities for the path-dependent inelastic GTN model, whose accuracy is further verified by the central difference method. The developed framework is utilized to design systems with prescribed plastic dissipation capacities while constraining the overall damage due to the ductile fracture mechanisms. A number of examples are considered to show the efficacy of the proposed topology optimization framework for obtaining failure resistant plastic energy-dissipating systems.

GTN Model with Shear Failure Modifications

GTN Constitutive Model

In the context of small strain plasticity theory, the strain tensor $\boldsymbol{\varepsilon}$ is additively decomposed into elastic ($\boldsymbol{\varepsilon}^e$) and plastic ($\boldsymbol{\varepsilon}^p$) components as

$$\boldsymbol{\varepsilon} = \boldsymbol{\varepsilon}^e + \boldsymbol{\varepsilon}^p \tag{1}$$

and the Cauchy stress $\boldsymbol{\sigma}$ is obtained by assuming the isotropic material behavior as

$$\boldsymbol{\sigma} = \mathbb{C}^e : \boldsymbol{\varepsilon}^e \tag{2}$$

where $\mathbb{C}^e = 3\kappa\mathbb{P}_{vol} + 2\mu\mathbb{P}^s_{dev}$ is the 4th order isotropic elasticity tensor; κ and μ = bulk and shear moduli, respectively; $\mathbb{P}_{vol}$ and $\mathbb{P}^s_{dev}$ = fourth-order volumetric and symmetric deviatoric projectors, respectively. The yield function of GTN model is expressed as

$$\phi(\boldsymbol{\sigma}, f, \zeta) = \frac{\sigma_v^2}{\zeta^2} + 2q_1 f^* \cosh\left(\frac{3q_2}{2}\frac{p}{\zeta}\right) - (1 + q_3 f^{*2}) = 0 \tag{3}$$

where σ_v = effective Mises stress; $p = \frac{1}{3}\boldsymbol{\sigma}:\boldsymbol{I}$ = mean stress (i.e., pressure); $\zeta(\alpha) = \sigma_y + \alpha K^h$ is the linear hardening function expressed in terms of the effective plastic strain α and hardening modulus K^h; q_1, q_2, and q_3 = three void interaction parameters; f = void volume fraction; and f^* = effective void volume fraction defined as

$$f^* = \begin{cases} f_{v0} & \text{virgin material} \\ f & f \le f_c \\ f_c + \dfrac{\bar{f}_u - f_c}{f_f - f_c}(f - f_c) & f_c < f < f_f \\ \bar{f}_u & f \ge f_f \text{(material failure)} \end{cases} \tag{4}$$

where f_{v0} = initial void volume fraction of the virgin material; f_c = void volume fraction at coalescence; f_f = void volume fraction at fracture initiation; and $\bar{f}_u$ = ultimate void volume fraction at failure where the material loses the load carrying capacity and is given by

$$\bar{f}_u = \frac{q_1 + \sqrt{q_1^2 - q_3}}{q_3} \tag{5}$$

The main purpose of introducing f^* in Eq. (4) is to simulate the rapid loss of load carrying capacity that accompanies the void coalescence stage of ductile fracture. When $f \le f_c$, f^* is governed by the void growth and nucleation and when $f > f_c$, f^* increases rapidly due to void coalescence. Finally, a complete failure at a material point occurs when f^* reaches $\bar{f}_u$. Therefore, f^* can be considered as the *effective damage* parameter in the GTN model.

With $\boldsymbol{s} = \boldsymbol{\sigma} - p\boldsymbol{I}$, denoting the deviatoric stress tensor, the yield surface in Eq. (3) can be expressed as

$$\phi(\boldsymbol{\sigma}, f, \zeta) = \frac{1}{2}\boldsymbol{s}:\boldsymbol{s} - \frac{1}{3}\left[1 + q_3 f^{*2} - 2q_1 f^* \cosh\left(\frac{3q_2}{2}\frac{p}{\zeta}\right)\right]\zeta^2 = 0 \tag{6}$$

J. Struct. Eng., 2020, 146(11): 04020229

According to the hypothesis of generalized normality, the plastic strain flow is assumed to be normal to the yield surface in Eq. (6) and is given by

$$\dot{\boldsymbol{\varepsilon}}^p = \gamma \frac{\partial \phi}{\partial \boldsymbol{\sigma}} = \gamma \left[\boldsymbol{s} + \frac{1}{3} q_1 q_2 f^* \zeta \sinh\left(\frac{3q_2}{2} \frac{p}{\zeta} \right) \boldsymbol{I} \right] \tag{7}$$

where γ = plastic multiplier. The macroscopic equivalent plastic strain flow $\dot{\alpha}$ is related to the microscopic values by the following relationship

$$\dot{\alpha} = \frac{\boldsymbol{\sigma} : \dot{\boldsymbol{\varepsilon}}^p}{(1-f)\zeta} = \frac{\gamma}{1-f} \left[\frac{1}{\zeta} \boldsymbol{s} : \boldsymbol{s} + q_1 q_2 p f^* \sinh\left(\frac{3q_2}{2} \frac{p}{\zeta} \right) \right] \tag{8}$$

In the original GTN model, the void volume fraction evolution was assumed to only consist of void nucleation and growth. Later, to account for damage due to void shearing effects at low-stress triaxialities, based on the studies by Bao and Wierzbicki (2004) and Barsoum and Faleskog (2007), Nahshon and Hutchinson (2008) modified the GTN model to incorporate the effect of Lode parameter that accounts for the damage due to void shearing at low-stress triaxiality. Thus, the void volume fraction in the GTN model was modified by adding an additional term to the void growth rate that depends on the Lode parameter. Finally, the evolution of the void volume fraction is characterized by existing voids growth $\dot{f}_g$, new void nucleation $\dot{f}_n$, and void shear $\dot{f}_s$ as

$$\dot{f} = \dot{f}_g + \dot{f}_n + \dot{f}_s \tag{9}$$

The growth of the existing voids $\dot{f}_g$ is based on the law of conservation of mass that is expressed in terms of the void volume fraction as

$$\dot{f}_g = (1-f)\dot{\boldsymbol{\varepsilon}}^p : \boldsymbol{I} = \gamma (1-f) q_1 q_2 \zeta f^* \sinh\left(\frac{3q_2}{2} \frac{p}{\zeta} \right) \tag{10}$$

It is more challenging to characterize the voids nucleation rate $\dot{f}_n$ because of the physically complex microstructures and inclusions. An effective and widely used statistical form for the nucleation rate was proposed by Chu and Needleman (1980) and is given by

$$\dot{f}_n = A(\alpha)\dot{\alpha} \tag{11}$$

where

$$A(\alpha) = \frac{f_N}{s_N \sqrt{2\pi}} \exp\left[-\frac{1}{2} \left(\frac{\alpha - \varepsilon_N}{s_N} \right)^2 \right] \tag{12}$$

in which f_N = volume fraction of the nucleated voids, the nucleation function A/f_N is assumed to have a normal distribution, with a mean value ε_N and standard deviation s_N. Note that the void nucleation is only considered under hydrostatic tension, i.e., when $p > 0$.

The modified flow term $\dot{f}_s$ to capture the void shearing effects in the low-stress triaxiality regime is expressed in terms of Lode parameter ($L = -\frac{27 J_3}{2\sigma_v^3}$) as

$$\dot{f}_s = k_\omega \omega_0 f \frac{\boldsymbol{s} : \dot{\boldsymbol{\varepsilon}}^p}{\sigma_v} = \sqrt{\frac{2}{3}} \gamma k_\omega \omega_0 f \|\boldsymbol{s}\| \tag{13}$$

with

$$\omega_0 = \omega(\boldsymbol{\sigma})\Gamma(\eta) \tag{14}$$

where

$$\omega(\boldsymbol{\sigma}) = 1 - \left(\frac{27 J_3}{2\sigma_v^3} \right)^2 \quad \text{and} \quad J_3 = \det(\boldsymbol{s}) \tag{15}$$

The threshold function $\Gamma(\eta)$ in Eq. (14) was introduced by Nielsen and Tvergaard (2010) to remove the void shearing effects at moderate- and high-stress triaxialities, which reads

$$\Gamma(\eta) = \begin{cases} 1 & \eta < \eta_1 \\ \dfrac{\eta - \eta_2}{\eta_1 - \eta_2} & \eta_1 \le \eta \le \eta_2 \\ 0 & \eta > \eta_2 \end{cases} \tag{16}$$

where $\eta = p/\sigma_v$ = stress triaxiality; and η_1 and η_2 = two stress triaxialities thresholds from where the shear modification effect starts to decay and completely becomes zero.

Finally, the constitutive model is completed by introducing the Karush–Kuhn–Tucker (KKT) and consistency conditions to describe the plastic loading and unloading as

$$\begin{aligned} &\gamma \ge 0, \phi \le 0, \gamma\phi = 0 \text{ (KKT conditions)} \\ &\gamma\dot{\phi} = 0 \text{ (Consistency condition)} \end{aligned} \tag{17}$$

The presented GTN model is implemented in the strain-driven finite element analysis (FEA) framework, and the implicit backward Euler scheme is adopted to discretize the evolution equations. A standard elastic predictor/return-mapping algorithm is used to solve the local nonlinear problem (de Souza Neto et al. 2011). Model implementation details in the context of FEA and the associated consistent algorithmic tangent modulus are provided in the Supplemental Materials.

Damage Constrained Topology Optimization

Design Parameterization

A density-based topology optimization is considered, and a density variable ρ_e is assigned to each finite element e to denote the presence ($\rho_e = 1$) or absence ($\rho_e = 0$) of material in an element. The density variables are relaxed to $\rho_e \in [0, 1]$ such that the gradient-based optimizers can be used. The constitutive material properties for an element are then expressed in terms of element density ρ_e. In particular, based on the solid isotropic material with penalization (SIMP) method (Bendsøe and Sigmund 1999), the Young's modulus E_e, yield stress σ_{y_e} and hardening modulus K_e^h for eth element with density ρ_e are interpolated as

$$\begin{aligned} E_e &= E_{\min} + (E_0 - E_{\min})\rho_e^{p_1} \\ \sigma_{y_e} &= \sigma_{y_{\min}} + (\sigma_{y_0} - \sigma_{y_{\min}})\rho_e^{p_2} \\ K_e^h &= K_{\min}^h + (K_0^h - K_{\min}^h)\rho_e^{p_3} \end{aligned} \tag{18}$$

where the parameters with subscript "*min*" and "0" = values for void and solid elements, respectively; and p_1, p_2, and p_3 = corresponding penalty factors. The material interpolation scheme given in Eq. (18) penalizes the plastic work in intermediate-density elements, making the intermediate-density or grey elements less efficient in dissipating plastic work, which can be then removed by the optimizer. However, large inelastic strains and damage can still occur in these intermediate-density elements and may

cause convergence issues in the global Newton-Raphson (NR) solver, especially in the early stages of optimization. To address this issue, different void element material properties, i.e., $E_{\min} = 10^{-8}E_0$, $\sigma_{y_{\min}} = 10^{-3}\sigma_{y_0}$, $K^h_{\min} = 10^{-3}K^h_0$, and penalty factors, i.e., $p_1 = 5$, $p_2 = p_3 = 4.5$, are used to delay the development of high plastic strains and damage in low-density elements. In addition, the following scaling scheme is considered to suppress the development of damage in the early stages of the optimization process

$$\dot{f}_{e_r} = \rho_e^{p_4}(\dot{f}_{g_{e_r}} + \dot{f}_{n_{e_r}} + \dot{f}_{s_{e_r}}) \tag{19}$$

where the subscript e_r = rth integration point in the eth element; p_4 = penalty factor that is set as 3 at the beginning of optimization iterations and is decreased by 0.1 every 10 iterations until it reaches the final value of 0 at the 300th iteration. By using this scaling and continuation scheme, the convergence issues in the global NR solver in the early stages of the optimization can be addressed. Moreover, there are no scaling effects on the actual damage in the final optimized topologies.

Optimization Problem Formulation

The optimization problem is formulated to seek minimum volume (or weight) structural designs that can dissipate the prescribed amount of plastic work with appropriate constraints on the damage. The optimization problem is formulated as

$$\begin{aligned}
\min_{\mathbf{0}\le \boldsymbol{x}\le \mathbf{1}} \quad & f_0(\boldsymbol{x}) = \frac{1}{V_0}\left(\sum_{e=1}^{n_{ele}} \rho_e(\boldsymbol{x}) V_e\right) \\
\text{s.t.} \quad & f_1(\boldsymbol{x}) = 1 - \frac{W^p(\boldsymbol{x})}{\bar{W}^p} \le 0 \\
& f_2(\boldsymbol{x}) = \frac{D_{\max}(\boldsymbol{x})}{\bar{D}} - 1 \le 0 \\
& \boldsymbol{R}^k(\boldsymbol{u}^k, \boldsymbol{u}^{k-1}, \boldsymbol{v}^k, \boldsymbol{v}^{k-1}, \boldsymbol{\rho}) = \mathbf{0} \\
& \boldsymbol{H}^k(\boldsymbol{u}^k, \boldsymbol{u}^{k-1}, \boldsymbol{v}^k, \boldsymbol{v}^{k-1}, \boldsymbol{\rho}) = \mathbf{0}
\end{aligned} \tag{20}$$

where n_{ele} = total number of elements in the design domain; V_0 = total design domain volume; V_0 = element volume; $\bar{W}^p$ = prescribed plastic work to be dissipated; and $\bar{D}$ = prescribed allowable damage. In this density-based formulation, the design variables $\boldsymbol{x}$ are related to the density variables $\boldsymbol{\rho}$ by a density filter that is used for regularizing the problem to remedy the checkerboarding and mesh-dependency issues (Bourdin 2001; Bruns and Tortorelli 2001). The density filter can be expressed in a matrix form as

$$\boldsymbol{\rho} = \boldsymbol{W}\boldsymbol{x} \tag{21}$$

where $\boldsymbol{\rho}$ and $\boldsymbol{x}$ = vectors collecting all the density and design variables, respectively; $\boldsymbol{W}$ = filtering matrix with the following components

$$W_{ej} = \frac{w_{ej}V_j}{\sum_{j=1}^{n_{ele}} w_{ej}V_j} \tag{22}$$

where V_j = volume of element j; and w_{ej} = distance weighting coefficient defined as

$$w_{ej} = \max\{r_{\min} - \|\boldsymbol{X}_e - \boldsymbol{X}_j\|_2, 0\} \tag{23}$$

in which $\boldsymbol{X}_e$ = centroid coordinate of element e; and $r_{\min}$ = prescribed density filter radius. The matrix $\boldsymbol{W}$ only needs to be calculated once and stored prior to the optimization process, and this stored information can be reused within each optimization iteration.

The plastic work dissipated in the design, $W^p(\boldsymbol{x})$, is computed using the trapezoidal rule as

$$W^p(\boldsymbol{x}) = \sum_{k=1}^{n}\left\{\sum_{e=1}^{n_{ele}}\left[\sum_{r=1}^{n_{ipt}} \frac{1}{2}(\boldsymbol{\sigma}^k_{e_r} + \boldsymbol{\sigma}^{k-1}_{e_r}) : (\boldsymbol{\varepsilon}^{p^k}_{e_r} - \boldsymbol{\varepsilon}^{p^{k-1}}_{e_r})\omega_{e_r}\right]\right\} \tag{24}$$

in which n_{ipt} = total number of integration point in an element; and $k = 1, 2, \ldots n$ = analysis steps during the application of load. Instead of enforcing local damage constraints at each integration point, which are computationally intractable, a single constraint on the aggregated maximum damage measure, $D_{\max}(\boldsymbol{x})$, within the entire domain is employed based on the p-norm approximation, which can be expressed as

$$D_{\max}(\boldsymbol{x}) = \left\{\sum_{e=1}^{n_{ele}}\left[\sum_{r=1}^{n_{ipt}} (\rho^q_e f^n_{e_r})^{p_n}\right]\right\}^{1/p_n} \tag{25}$$

where ρ^q_e = damage relaxation factor in terms of the density variable that is used to remove the spurious high damage in the intermediate-density elements (Li et al. 2017), enabling the convergence to discrete topologies; p_n = p-norm parameter; and $f^n_{e_r}$ = total effective damage, i.e. the effective void volume fraction at the integration point at the final step (step n). In this study, $q = 0$ is used for the first 500 iterations to allow the topology evolution driven by the actual damage, and $q = 3$ is used for the last 200 iterations to relax the damage in the intermediate-density elements in order to get the final discrete topologies.

To represent the physics of the underlying system, two sets of constraints $\boldsymbol{R}^k = 0$ and $\boldsymbol{H}^k = 0$, related to global system equilibrium and the GTN constitutive model, respectively, are needed to be satisfied at each analysis step k. A nested formulation is considered, and these constraints are handled outside the optimizer within FEA, as is customarily done in large-scale topology optimization (Christensen and Klarbring 2008). As shown in the Supplemental Materials, the global equilibrium constraints $\boldsymbol{R}^k = 0$ at step k are assembled using the elemental residuals $\boldsymbol{R}^k_e$ as

$$\boldsymbol{R}^k = \mathop{\mathcal{A}}_{e=1}^{n_{ele}} \boldsymbol{R}^k_e \quad \text{with} \quad \boldsymbol{R}^k_e = \boldsymbol{F}^{e^k}_{int} - \boldsymbol{F}^{e^k}_{ext} \tag{26}$$

where $\boldsymbol{F}^{e^k}_{ext}$ = external force that is equal to $\mathbf{0}$ in the displacement controlled strategy used in this study; and $\boldsymbol{F}^{e^k}_{int}$ = internal force that is expressed as

$$\boldsymbol{F}^{e^k}_{int} = \sum_{r=1}^{n_{ipt}} \boldsymbol{B}^T_{e_r}\boldsymbol{\sigma}^k_{e_r}\omega_{e_r} \tag{27}$$

in which $\boldsymbol{B}_{e_r}$ = shape function derivative matrix evaluated at the rth integration point of element e; and ω_{e_r} = corresponding weight. Using the framework for path-dependent topology optimization presented by (Alberdi et al. 2018), an auxiliary variable vector ($\boldsymbol{v}^k$) is introduced that consists of Cauchy stress tensor ($\boldsymbol{\sigma}^k_{e_r}$), plastic strain tensor ($\boldsymbol{\varepsilon}^{p^k}_{e_r}$), effective plastic strain ($\alpha^k_{e_r}$), void volume fraction ($f^k_{e_r}$), and plastic multiplier ($\Delta\gamma^k_{e_r}$) at a Gauss point as

$$\boldsymbol{v}^k = \begin{bmatrix} \boldsymbol{v}^k_1 \\ \vdots \\ \boldsymbol{v}^k_e \\ \vdots \\ \boldsymbol{v}^k_{n_{ele}} \end{bmatrix} \quad \text{with} \quad \boldsymbol{v}^k_e = \begin{bmatrix} \boldsymbol{v}^k_{e_1} \\ \boldsymbol{v}^k_{e_2} \\ \boldsymbol{v}^k_{e_3} \\ \boldsymbol{v}^k_{e_4} \end{bmatrix} \quad \text{and} \quad \boldsymbol{v}^k_{e_r} = \begin{bmatrix} \boldsymbol{\sigma}^k_{e_r} \\ \boldsymbol{\varepsilon}^{p^k}_{e_r} \\ \alpha^k_{e_r} \\ f^k_{e_r} \\ \Delta\gamma^k_{e_r} \end{bmatrix} \tag{28}$$

J. Struct. Eng., 2020, 146(11): 04020229

Accordingly, the local constraints $\boldsymbol{H}^k$ to be satisfied at each Gauss point are defined as

$$\boldsymbol{H}^k = \begin{bmatrix} \boldsymbol{H}_1^k \\ \vdots \\ \boldsymbol{H}_e^k \\ \vdots \\ \boldsymbol{H}_{n_{ele}}^k \end{bmatrix} \quad \text{with} \quad \boldsymbol{H}_e^k = \begin{bmatrix} \boldsymbol{H}_{e_1}^k \\ \boldsymbol{H}_{e_2}^k \\ \boldsymbol{H}_{e_3}^k \\ \boldsymbol{H}_{e_4}^k \end{bmatrix} \quad \text{and} \quad \boldsymbol{H}_{e_r}^k = \begin{bmatrix} \boldsymbol{h}_{e_1}^k \\ \boldsymbol{h}_{e_2}^k \\ h_{e_3}^k \\ h_{e_4}^k \\ h_{e_5}^k \end{bmatrix} \tag{29}$$

Based on the discrete material constitutive formulation given in the Supplemental Materials, for an elastic step, $\boldsymbol{H}_{e_r}^k$ is expressed as

$$\boldsymbol{H}_{e_r}^k = \begin{cases} \boldsymbol{h}_{e_{r1}}^k = \boldsymbol{\sigma}_{e_r}^k - \mathbb{C}^e{:}(\boldsymbol{\varepsilon}_{e_r}^k - \boldsymbol{\varepsilon}_{e_r}^{p^k}) = \boldsymbol{0} \\ \boldsymbol{h}_{e_{r2}}^k = \boldsymbol{\varepsilon}_{e_r}^{p^k} - \boldsymbol{\varepsilon}_{e_r}^{p^{k-1}} = \boldsymbol{0} \\ h_{e_{r3}}^k = \alpha_{e_r}^k - \alpha_{e_r}^{k-1} = 0 \\ h_{e_{r4}}^k = f_{e_r}^k - f_{e_r}^{k-1} = 0 \\ h_{e_{r5}}^k = \Delta\gamma_{e_r}^k = 0 \end{cases} \tag{30}$$

while for a plastic step, $\boldsymbol{H}_{e_r}^k$ is expressed as

$$\boldsymbol{H}_{e_r}^k = \begin{cases} \boldsymbol{h}_{e_{r1}}^k = \boldsymbol{\sigma}_{e_r}^k - \mathbb{C}^e{:}(\boldsymbol{\varepsilon}_{e_r}^k - \boldsymbol{\varepsilon}_{e_r}^{p^k}) = \boldsymbol{0} \\ \boldsymbol{h}_{e_{r2}}^k = \boldsymbol{\varepsilon}_{e_r}^{p^k} - \boldsymbol{\varepsilon}_{e_r}^{p^{k-1}} - \Delta\gamma_{e_r}^k \left(\boldsymbol{s}_{e_r}^k + \frac{1}{3} q_1 q_2 f_{e_r}^{*^k} \zeta_{e_r}^k \mathrm{SINH}_{e_r}^k \boldsymbol{I} \right) = \boldsymbol{0} \\ h_{e_{r3}}^k = \alpha_{e_r}^k - \alpha_{e_r}^{k-1} - \dfrac{\Delta\gamma_{e_r}^k}{1 - f_{e_r}^k} \left(\dfrac{1}{\zeta_{e_r}^k} \boldsymbol{s}_{e_r}^k{:}\boldsymbol{s}_{e_r}^k + q_1 q_2 p_{e_r}^k f_{e_r}^{*^k} \mathrm{SINH}_{e_r}^k \right) = 0 \\ h_{e_{r4}}^k = f_{e_r}^k - f_{e_r}^{k-1} - \Delta\gamma_{e_r}^k (B_{e_r}^k + C_{e_r}^k + D_{e_r}^k) = 0 \\ h_{e_{r5}}^k = \dfrac{1}{2} \boldsymbol{s}_{e_r}^k{:}\boldsymbol{s}_{e_r}^k - \dfrac{1}{3} (1 + q_3 f_{e_r}^{*^{k^2}} - 2 q_1 f_{e_r}^{*^k} \mathrm{COSH}_{e_r}^k) \zeta_{e_r}^{k^2} = 0 \end{cases} \tag{31}$$

where $\mathrm{SINH} = \sinh\left(\frac{3q_2}{2}\frac{p}{\zeta}\right)$ and $\mathrm{COSH} = \cosh\left(\frac{3q_2}{2}\frac{p}{\zeta}\right)$. Here, $\boldsymbol{h}_{e_1}^k$ = stress-strain relationship; while $\boldsymbol{h}_{e_2}^k$, $h_{e_3}^k$, and $h_{e_4}^k$ = updates for plastic strain, effective plastic strain, and void volume fraction, respectively; $h_{e_5}^k$ = yield function of the GTN model. The explicit expressions of variables B, C, and D are given in the Supplemental Materials.

Sensitivity Analysis

As the number of design variables in topology optimization is much greater than the number of objective and constraint functions, the adjoint sensitivity analysis framework proposed by Alberdi et al. (2018) for transient nonlinear coupled systems is adopted in this work for deriving the analytical design sensitivities for the considered GTN model. Consider a general objective or constraint function $F(\boldsymbol{u}^k, \ldots, \boldsymbol{u}^1, \boldsymbol{v}^k, \ldots, \boldsymbol{v}^1, \boldsymbol{\rho})$ in terms of the solution field variable $\boldsymbol{u}^k$, auxiliary variable $\boldsymbol{v}^k$, and density variable $\boldsymbol{\rho}$. An augmented function $\hat{F}$ is first constructed as follows

$$\hat{F} = F + \sum_{k=1}^{n} \boldsymbol{\lambda}^{k^T} \boldsymbol{R}^k(\boldsymbol{u}^k, \boldsymbol{u}^{k-1}, \boldsymbol{v}^k, \boldsymbol{v}^{k-1}, \boldsymbol{\rho}) + \sum_{k=1}^{n} \boldsymbol{\mu}^{k^T} \boldsymbol{H}^k(\boldsymbol{u}^k, \boldsymbol{u}^{k-1}, \boldsymbol{v}^k, \boldsymbol{v}^{k-1}, \boldsymbol{\rho}) \tag{32}$$

where $\boldsymbol{\lambda}^k$ and $\boldsymbol{\mu}^k$ = adjoint multipliers associated with constraints $\boldsymbol{R}^k = \boldsymbol{0}$ and $\boldsymbol{H}^k = \boldsymbol{0}$, respectively. Taking the derivative of $\hat{F}$ with respect to $\boldsymbol{\rho}$ and eliminating all the coefficients that contain the implicit derivative terms, $d\boldsymbol{u}^k/d\boldsymbol{\rho}$ and $d\boldsymbol{v}^k/d\boldsymbol{\rho}$, yields

$$\frac{d\hat{F}}{d\boldsymbol{\rho}} = \frac{dF}{d\boldsymbol{\rho}} = \frac{\partial F}{\partial \boldsymbol{\rho}} + \sum_{k=1}^{n} \left(\boldsymbol{\lambda}^{k^T} \frac{\partial \boldsymbol{R}^k}{\partial \boldsymbol{\rho}} + \boldsymbol{\mu}^{k^T} \frac{\partial \boldsymbol{H}^k}{\partial \boldsymbol{\rho}} \right) \tag{33}$$

where the unknowns $\boldsymbol{\lambda}^k$ and $\boldsymbol{\mu}^k$ are obtained by solving the adjoint systems in a backward manner (from $k = n$ to $k = 1$) as

$$\text{step } n: \begin{cases} \dfrac{\partial F}{\partial \boldsymbol{u}^n} + \boldsymbol{\lambda}^{n^T} \dfrac{\partial \boldsymbol{R}^n}{\partial \boldsymbol{u}^n} + \boldsymbol{\mu}^{n^T} \dfrac{\partial \boldsymbol{H}^n}{\partial \boldsymbol{u}^n} = \boldsymbol{0} \\ \dfrac{\partial F}{\partial \boldsymbol{v}^n} + \boldsymbol{\lambda}^{n^T} \dfrac{\partial \boldsymbol{R}^n}{\partial \boldsymbol{v}^n} + \boldsymbol{\mu}^{n^T} \dfrac{\partial \boldsymbol{H}^n}{\partial \boldsymbol{v}^n} = \boldsymbol{0} \end{cases}$$

$$\text{step } k: \begin{cases} \dfrac{\partial F}{\partial \boldsymbol{u}^k} + \boldsymbol{\lambda}^{k+1^T} \dfrac{\partial \boldsymbol{R}^{k+1}}{\partial \boldsymbol{u}^k} + \boldsymbol{\mu}^{k+1^T} \dfrac{\partial \boldsymbol{H}^{k+1}}{\partial \boldsymbol{u}^k} + \boldsymbol{\lambda}^{k^T} \dfrac{\partial \boldsymbol{R}^k}{\partial \boldsymbol{u}^k} + \boldsymbol{\mu}^{k^T} \dfrac{\partial \boldsymbol{H}^k}{\partial \boldsymbol{u}^k} = \boldsymbol{0} \\ \dfrac{\partial F}{\partial \boldsymbol{v}^k} + \boldsymbol{\lambda}^{k+1^T} \dfrac{\partial \boldsymbol{R}^{k+1}}{\partial \boldsymbol{v}^k} + \boldsymbol{\mu}^{k+1^T} \dfrac{\partial \boldsymbol{H}^{k+1}}{\partial \boldsymbol{v}^k} + \boldsymbol{\lambda}^{k^T} \dfrac{\partial \boldsymbol{R}^k}{\partial \boldsymbol{v}^k} + \boldsymbol{\mu}^{k^T} \dfrac{\partial \boldsymbol{H}^k}{\partial \boldsymbol{v}^k} = \boldsymbol{0} \end{cases} \tag{34}$$

By inspecting Eqs. (33) and (34), the following explicit derivatives are needed to complete the adjoint sensitivity analysis

$$\begin{aligned} &\text{For } F\text{: } \frac{\partial F}{\partial \boldsymbol{\rho}}, \frac{\partial F}{\partial \boldsymbol{u}^k}, \frac{\partial F}{\partial \boldsymbol{v}^k} \\ &\text{For } \boldsymbol{R}^k\text{: } \frac{\partial \boldsymbol{R}^k}{\partial \boldsymbol{\rho}}, \frac{\partial \boldsymbol{R}^k}{\partial \boldsymbol{u}^k}, \frac{\partial \boldsymbol{R}^k}{\partial \boldsymbol{u}^{k-1}}, \frac{\partial \boldsymbol{R}^k}{\partial \boldsymbol{v}^k}, \frac{\partial \boldsymbol{R}^k}{\partial \boldsymbol{v}^{k-1}} \\ &\text{For } \boldsymbol{H}^k\text{: } \frac{\partial \boldsymbol{H}^k}{\partial \boldsymbol{\rho}}, \frac{\partial \boldsymbol{H}^k}{\partial \boldsymbol{u}^k}, \frac{\partial \boldsymbol{H}^k}{\partial \boldsymbol{u}^{k-1}}, \frac{\partial \boldsymbol{H}^k}{\partial \boldsymbol{v}^k}, \frac{\partial \boldsymbol{H}^k}{\partial \boldsymbol{v}^{k-1}} \end{aligned} \tag{35}$$

Detailed expressions for the presented explicit derivatives are provided in the Supplemental Materials.

Numerical Examples

Numerical examples are presented in this section to demonstrate the proposed method. All the examples are discretized by 8-node

quadrilateral elements of 10-mm thickness with four Gauss integration points. The matrix material parameters are set as Young's modulus $E = 210$ GPa, Poisson's ratio $\nu = 0.3$, initial yield strength $\sigma_y = 370$ MPa, and linear hardening modulus $K^h = 4.2$ GPa. For GTN model parameters, the initial void volume is chosen as $f_{v0} = 0.001$, together with the void interaction parameters $q_1 = 1.5$, $q_2 = 1.0$, and $q_3 = 2.25$. The shear modification factors are assumed to be $k_\omega = 3$, $\eta_1 = 0$ and $\eta_2 = 0.5$. The void volume fraction is set to $f_c = 0.05$ at coalescence and $f_f = 0.3$ at fracture initiation. The voids are nucleated with $f_N = 0.04$ with a standard deviation of $s_N = 0.1$ and a mean nucleation strain of $\varepsilon_N = 0.35$. According to Eqs. (4) and (5), the ultimate void volume fraction at material failure is $f^* = \bar{f}_u = 0.6667$. The choice of the GTN model parameters is based on the calibration results of various metals, as summarized in (Kiran and Khandelwal 2014; Nielsen and Tvergaard 2010). The p-norm parameter is set to $p_n = 20$ based on numerical testing as it yields best designs for the considered problems and parameter settings. In practice, different values of p_n should be considered to determine the appropriate p-norm parameter for the problem under consideration.

All the optimizations initiate with a fully solid design, i.e., $\rho_e = 1$. The method of moving asymptotes (MMA) (Svanberg 1987) is used as an optimizer with default settings, and all the optimizations are terminated after 700 iterations. The optimized designs are obtained with different prescribed plastic work $\bar{W}_p$ and damage constraint values such that $\bar{D} \le f_c = 0.05$ in Eq. (20), as the failure occurs quickly after the void coalescence condition is met. The performance of damage constrained topologies are also compared with the von Mises (J_2 plasticity) designs, which are obtained by setting $f_{v0} = q_1 = q_3 = f_N = k_\omega = 0$ in the GTN model, as the von Mises model is a special case of the GTN model. All the presented plastic work distributions are with unit J/mm^2, while stress triaxiality and damage plots are dimensionless [-]. Since the goal of optimization is to constrain the damage below the void coalescence threshold (f_c), the void coalescence term [Eq. (4)] in the GTN model is turned off for topology optimization by enforcing $f^* = f$. Accordingly, f^* is replaced by f in all FEA and optimization processes. This helps to prevent failure related convergence issues in the global NR solver in the intermediate optimization iterations. However, all the ultimate performance analyses for the evaluation of optimized designs consider this void coalescence effect. The implemented adjoint path-dependent sensitivity analysis is verified by the central difference method before being used for topology optimization, see the Supplemental Materials for more details. All the FEAs and optimizations are carried out using an in-house Matlab based finite element library *CPSSL-FEA* developed at the University of Notre Dame.

Short Cantilever Beam—Triaxiality Dominated Design

The performance of the proposed method is first tested on the design of a cantilever beam, as shown in Fig. 1(a). A downward displacement $u = 25$ mm is applied along 6 mm at the center of the right edge. The design domain is discretized by a 100×50 mesh. The minimum plastic work to be dissipated is $\bar{W}^p = 980$ J, and the density filter radius is set to $r_{\min} = 2$ mm.

As a reference design, the optimized topology with the von Mises model is first generated. In this case, the minimum volume structure is sought to dissipate the target amount of plastic work, and there are no damage constraints as the damage is not considered in the von Mises plasticity. The optimized design is shown in Fig. 1(b), and this figure shows that a symmetric design about the central horizontal axis is obtained with an optimized volume fraction of $f_0 = 0.6345$. This is as expected as the von Mises yield criterion is pressure independent, resulting in symmetric displacement and plastic strain fields, further leading to symmetric sensitivities and eventually a symmetric design. However, when this optimized design is reanalyzed with the GTN model, it cannot sustain the design displacement of $u = 25$ mm, as the material failure ($f^* = \bar{f}_u = 0.6667$) occurs before the design displacement is reached. As indicated in Table 1, the ductility, i.e., displacement at the failure point, of the von Mises design is only 16.23 mm with 45.00 kN load carrying capacity, resulting in only 551.56 J of plastic energy dissipation, which is far below the prescribed value of 980 J. The corresponding field distributions of the reanalyzed results with the GTN model at the failure point are shown in Figs. 1(c–e). Fig. 1(c) shows that the plastic work is mostly

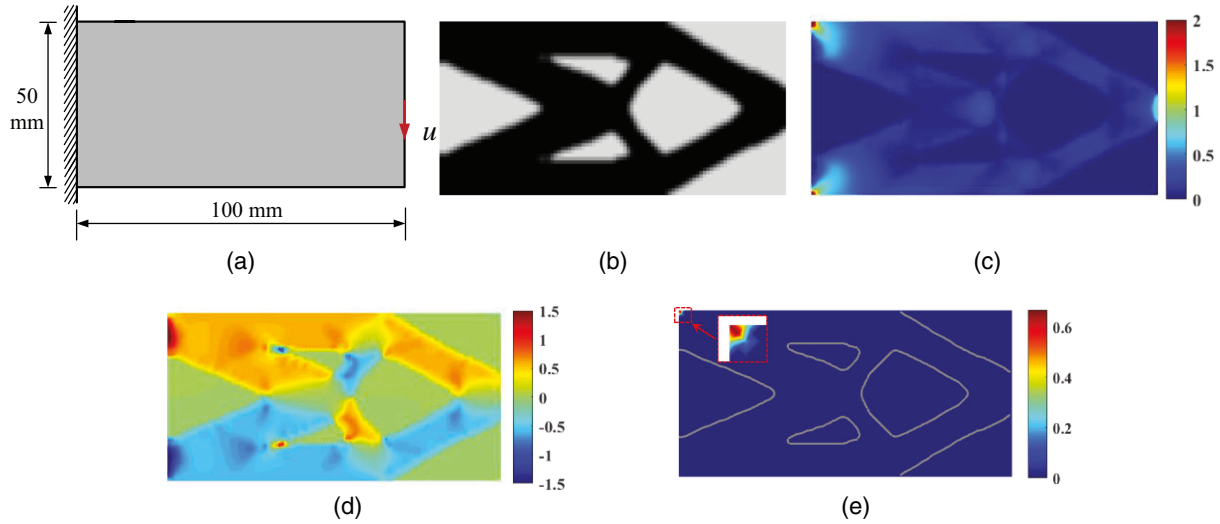

Fig. 1. Optimized cantilever beam design using the von Mises model and the corresponding field distributions reanalyzed by the GTN model up to the failure point: (a) design domain; (b) von Mises design, $f_0 = 0.6345$; (c) plastic work, $W_{ult}{}^p = 551.56$ J; (d) stress triaxiality; and (e) effective damage, $f^*_{max} = 0.6667$.

Table 1. Performance comparison of the optimized cantilever beam designs

Figure No.	Model	$\bar{D}$	Volume fraction	Ductility (mm)	Load carrying capacity (kN)	W^p_{ult} (J)
Fig. 1(b)	von Mises	N/A	0.6345	16.23	45.00	551.56
Fig. 3(a)	GTN	0.01	0.6502	47.97	75.62	2,445.90

concentrated at the top and bottom left corners, and the material failure is initiated at the top left corner [Fig. 1(e)] where the stress triaxiality is positive [Fig. 1(d)].

To further understand the governing failure mechanisms in the von Mises design, the distributions of each contributor to the maximum damage $f = 0.3024$, leading to the effective damage $f^* = \bar{f}_u = 0.6667$, are plotted in Fig. 2. This figure shows that the void growth at the top left corner is the dominating failure mechanism with the damage value $f_{g_1} = 0.2508$. This is because of high inelastic strains and positive stress triaxiality at this location, as indicated in Figs. 1(c and d). Moreover, due to the negative triaxiality, the void growth is suppressed $f_{g_2} = -0.0013$ at the bottom left corner, and void closure occurs at this location, compensating for the other damage mechanism, i.e., shear damage [$f_{s_2} = 0.0014$ in Fig. 2(c)], at this location. Void nucleation $f_{n_1} = 0.0516$ also contributes to the damage at the top left corner, but the void nucleation is absent at the bottom left corner, which is mostly under compression. In contrast, the shear damage at the top left corner is zero due to the high-stress triaxiality at this location.

To mitigate the damage under the design displacement while still dissipating the prescribed amount of plastic work, the optimized design with the GTN model with $\bar{D} = 0.01$ is obtained and shown in Fig. 3(a). The figure shows that more material is needed, i.e., $f_0 = 0.6502$, to satisfy the damage constraint in this case, and the resulting topology is no longer symmetric. This is because this asymmetric design results in a better distribution of plastic work [Fig. 3(b)] and stress triaxiality [Fig. 3(c)], ending up being feasible ($f^*_{\max} = 0.0094 < \bar{D} = 0.01 < f_c = 0.05$), with more evenly distributed damage [Fig. 3(d)].

The convergence histories of the objective and constraints, as well as several intermediate topologies, are shown in Fig. 4. Several oscillations can be seen in the first 30 iterations. This is primarily due to the appearance of large grey areas in the early iterations, resulting in constraint violations. Nevertheless, due to the scaling and continuation schemes used in this study, no FEA convergence issues were encountered in this stage. Once the overall structural topology is determined after the first 50 iterations, the convergence becomes smoother except for the spikes when the scaling parameter p_4 is updated. Fig. 4(b) shows that all the constraints are satisfied

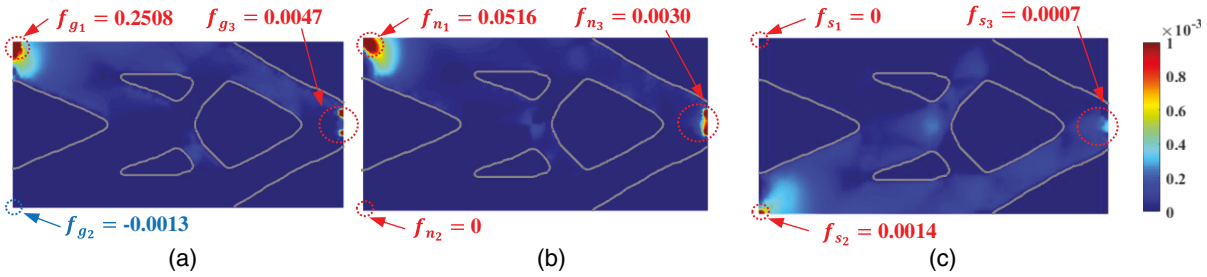

Fig. 2. Contributions of each damage mechanism for the von Mises cantilever beam design at the failure point (scales are adjusted for a better visualization): (a) Void growth f_g; (b) Void nucleation f_n; and (c) Void shear f_s.

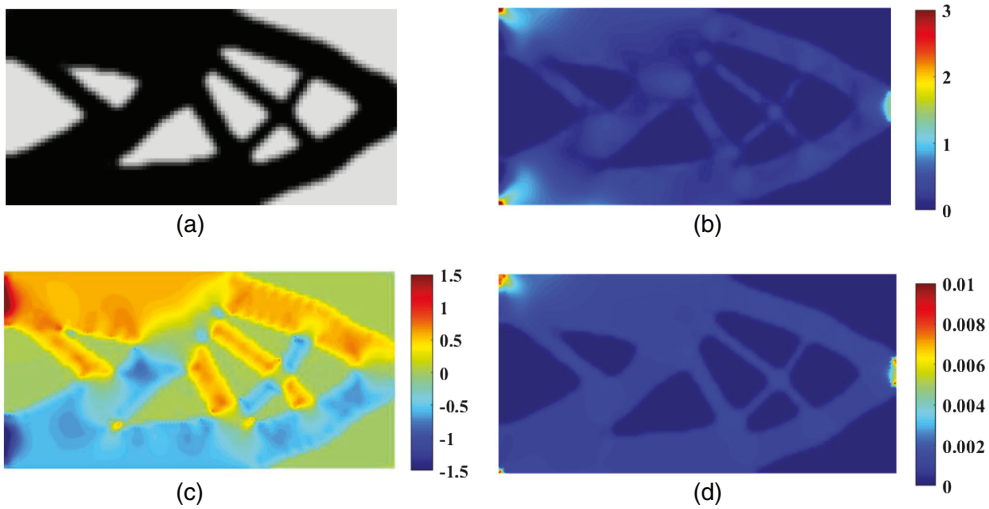

Fig. 3. Optimized cantilever beam design using the GTN model with $\bar{D} = 0.01$ and the corresponding field distributions: (a) GTN design, $f_0 = 0.6502$; (b) plastic Work $W^p = 980$ J; (c) stress triaxiality of GTN design; and (d) effective damage $f^*_{\max} = 0.0094$.

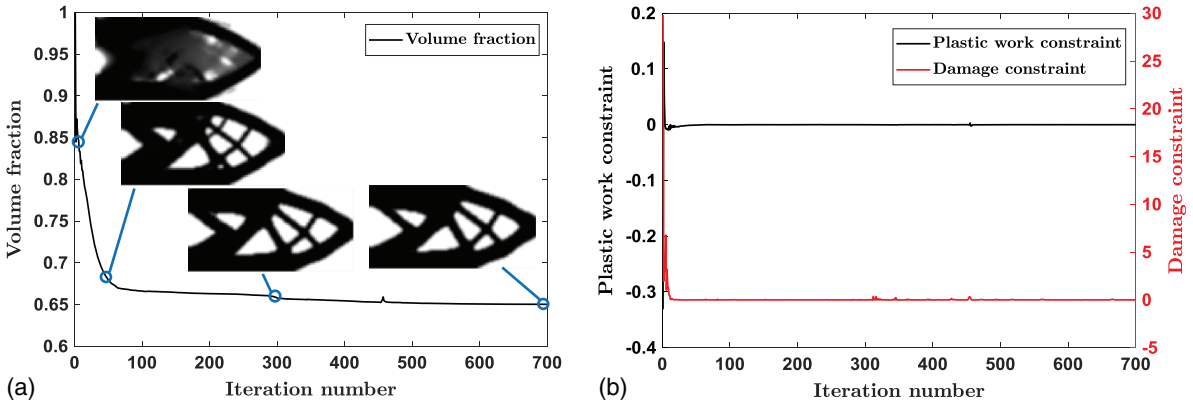

Fig. 4. Convergence histories of the cantilever beam design with the GTN model and $\bar{D} = 0.01$: (a) objective function and intermediate solutions; and (b) constraint functions.

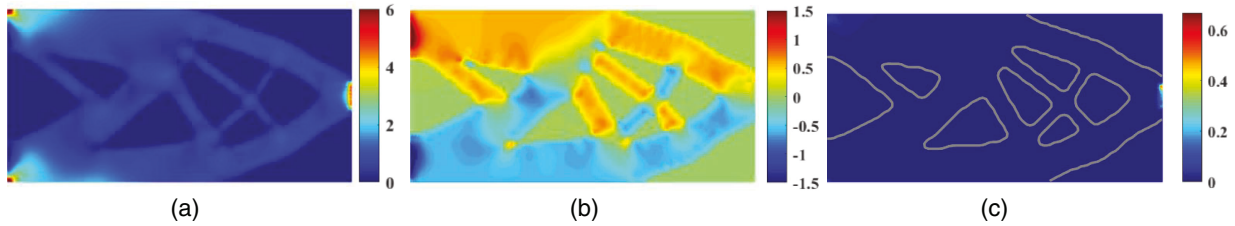

Fig. 5. Ultimate behavior of the optimized cantilever beam design with the GTN model at the failure point: (a) plastic work $W_{ult}{}^{p} = 2445.90$ J; (b) stress triaxiality of GTN design; and (c) effective damage, $f^{*}_{\max} = 0.6667$.

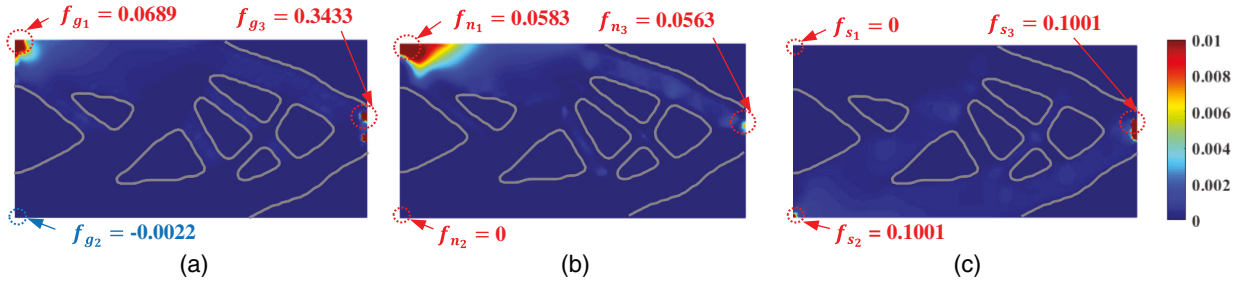

Fig. 6. Contributions of each damage mechanism for the GTN cantilever beam design at the failure point (scales are adjusted for a better visualization): (a) Void growth f_g; (b) Void nucleation f_n; and (c) Void shear f_s.

when the optimization is terminated after 700 iterations, and the final optimized design is feasible.

Fig. 5 shows the results corresponding to the ultimate behaviors of the topology obtained from the GTN model at the failure point. The figure shows that compared to the von Mises design [Fig. 1(c)], the plastic work dissipation in this topology [Fig. 5(a)] is more evenly distributed in the design domain, indicating a better utilization of material. Moreover, the final failure occurs in the region close to the application of loads instead of the support region in the von Mises design, as shown in Fig. 5(c). Fig. 6 shows that void growth is still the governing damage mechanism in this case with $f_{g_3} = 0.3433$ [Fig. 6(a)] at the failure initiation location. More importantly, the ductility of the GTN design is 47.97 mm with the ultimate energy dissipation capacity of 2445.90 J (Table 1), which is far better than the von Mises design with the ductility of 16.23 mm and ultimate energy dissipation capacity of 551.56 J. Better performance of the GTN design over the von Mises design can also be seen from the ultimate load-displacement curves of each design in Fig. 7. All the ultimate load-displacement curves are

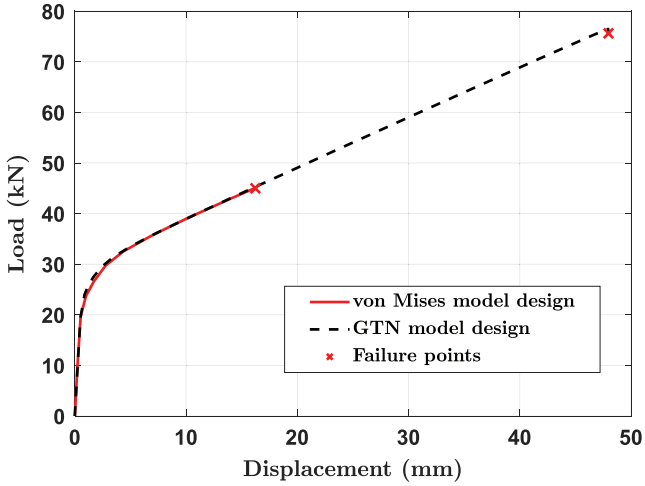

Fig. 7. Load-displacement curves for the optimized cantilever beam designs up to the failure points.

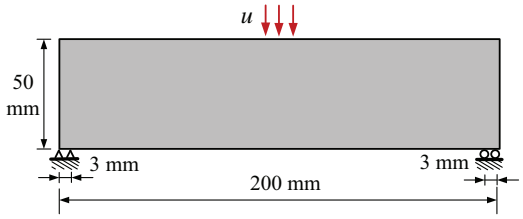

Fig. 8. Simply supported beam design domain.

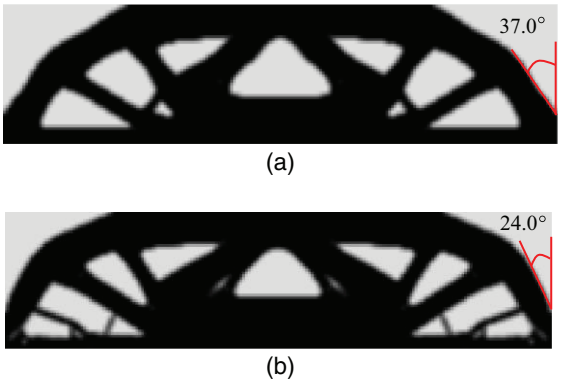

Fig. 9. Optimized designs with the von Mises and GTN models with $\bar{D} = 0.01$: (a) von Mises design, $f_0 = 0.6579$; and (b) GTN design, $\bar{D} = 0.01$, $f_0 = 0.7069$.

plotted up to the failure points, which are defined as the complete failure at any integration point. The ductility, load carrying capacity, and ultimate energy-dissipating capacity are evaluated at the failure point as the structural strength deteriorates rapidly after this point and the system is not able to safely dissipate energy.

Simply Supported Beam—Shear Dominated Design

In the second example, the design of a simply supported beam shown in Fig. 8 is considered. The design domain is subjected to a downward displacement of $u = 25$ mm applied along 4 mm in the middle of the top surface. Due to symmetry, only the left-half design domain with 100×50 finite element mesh and symmetric boundary conditions is optimized. The required minimum plastic work dissipation is $\bar{W}^p = 1000$ J, and the density filter radius is set to $r_{\min} = 2$ mm.

Figs. 9(a and b) show the optimized topologies with the von Mises model and GTN model subjected to prescribed allowable damage $\bar{D} = 0.01$, respectively. The figure shows that different designs are obtained in these cases, where the top left and right members in the von Mises design tend to be more vertical compared to the ones in the GTN design, i.e., 37.0° in Fig. 9(a) versus 24.0° in Fig. 9(b). However, more material is needed for GTN design (i.e., $f_0 = 0.7069$) to satisfy the prescribed damage constraint, as compared to the von Mises design with $f_0 = 0.6579$.

To further understand the topological changes brought by using the GTN model with damage constraint, the plastic work, stress triaxiality, and damage distributions of the optimized designs in Figs. 9(a and b) are shown in Fig. 10. In Fig. 10, the von Mises design is reanalyzed using the GTN model with the consideration of void coalescence. Fig. 10 shows that less amount of plastic energy (997.58 J < 1000 J) is dissipated, and the plastic work is mostly concentrated near the support regions in the von Mises design. The stress triaxiality plot shows that this region is mostly under negative stress triaxiality, indicating that the void shearing is the dominating failure mechanism in this case, which is different from the cantilever example where the void growth under positive stress triaxiality was the dominating mechanism. The damage plot reveals that the maximum effective damage $f^*_{\max} = 0.049$ is close to the coalescence threshold of $f_c = 0.05$, and therefore, the system is close to failure. The ultimate damage plots shown in Fig. 11 confirm that the shear damage ($f_s = 0.3095$) is the dominating failure mechanism in this design.

In contrast, the design obtained by the GTN model with maximum allowable damage of $\bar{D} = 0.01$ dissipates plastic energy more evenly through the entire structure by distributing the material in a more efficient way. The peak plastic energy in the support region is reduced from 5.35 J/mm^2 in the von Mises design to 2.70 J/mm^2 in the GTN design. Moreover, by placing the top end chord in a vertical manner, the magnitude of the maximum negative stress triaxiality is also reduced from −0.96 to −0.85 at the supports, as shown in the second column of Fig. 10. These topological changes

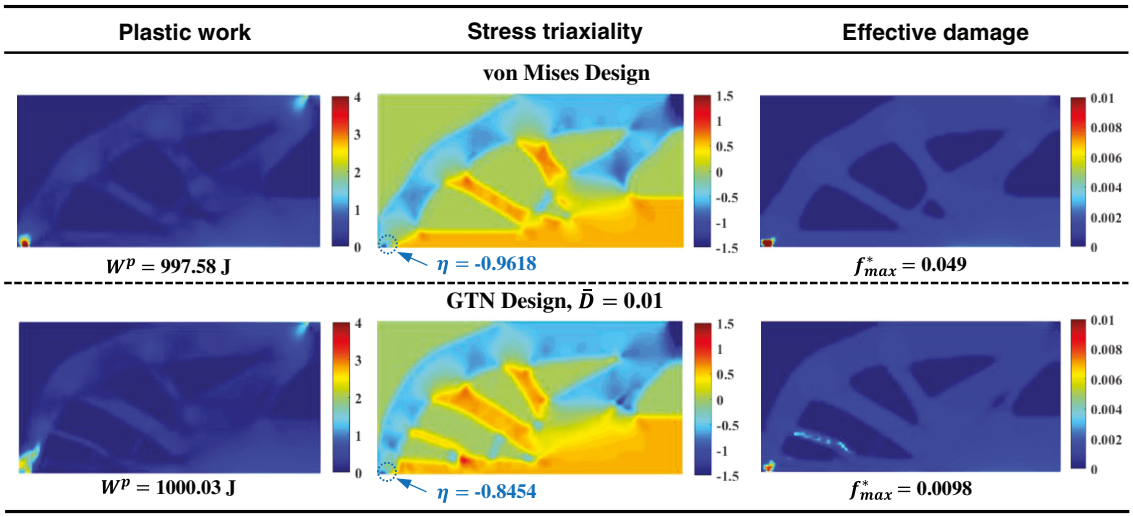

Fig. 10. Field distributions of the optimized simply supported beam designs at the design displacement.

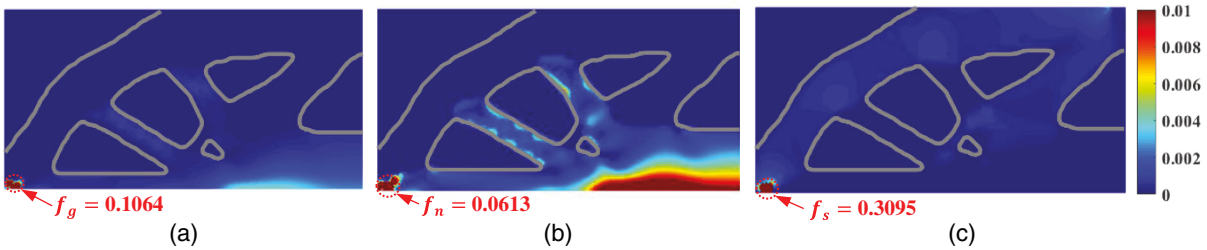

Fig. 11. Contributions of each damage mechanism for the von Mises simply supported beam design at the failure point (scales are adjusted for a better visualization): (a) void growth f_g; (b) void nucleation f_n; and (c) void shear f_s.

Table 2. Performance comparison of the optimized simply supported beam designs

Figure No.	Model	$\bar{D}$	Volume fraction	Ductility (mm)	Load carrying capacity (kN)	W^p_{ult} (J)
Fig. 9(a)	von Mises	N/A	0.6579	66.78	95.71	4,076.49
Fig. 9(b)	GTN	0.01	0.7069	97.12	123.42	7,376.36

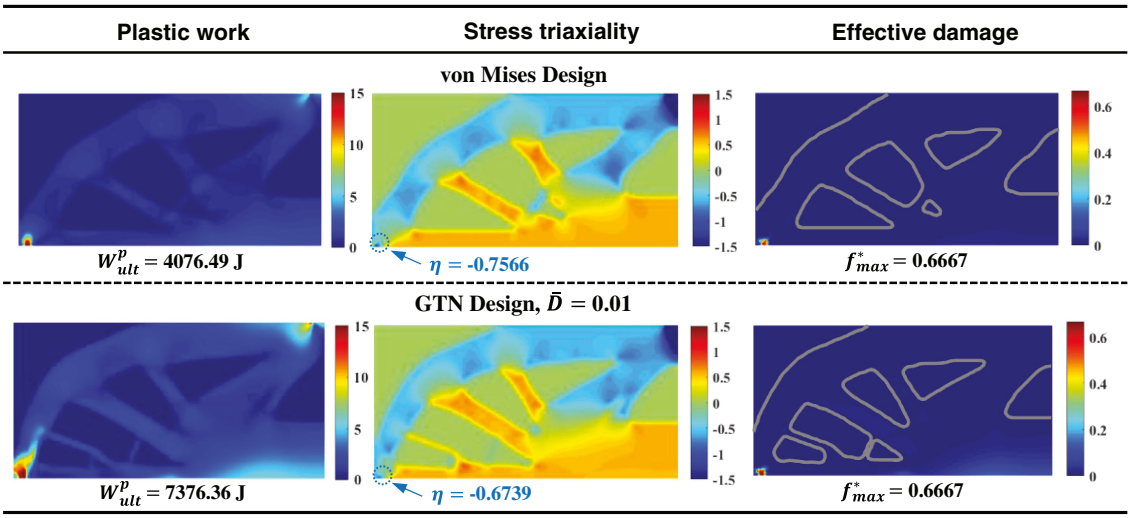

Fig. 12. Ultimate behaviors of the optimized simply supported beam designs at the failure points.

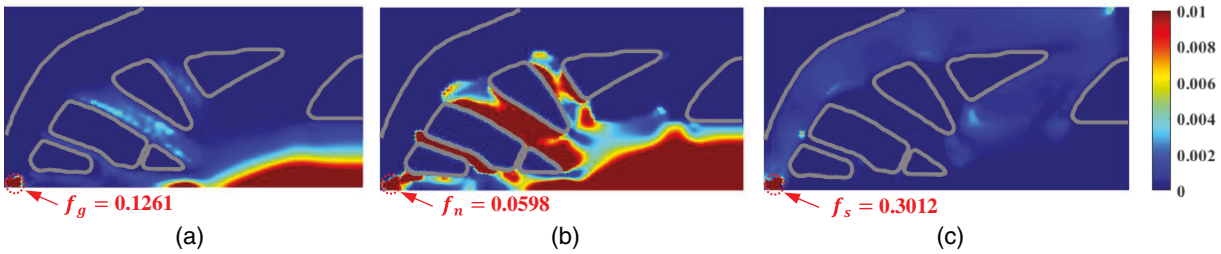

Fig. 13. Contributions of each damage mechanism for the GTN simply supported beam design at the failure point (scales are adjusted for a better visualization): (a) void growth $f_g = 0.1261$; (b) void nucleation f_n; and (c) void shear f_s.

result in a smaller effective damage, satisfying the prescribed damage constraint, i.e., $f^*_{\max} = 0.0098 < \bar{D} = 0.01$.

Finally, the two optimized designs are evaluated for their ultimate failure responses, and the results are summarized in Table 2. Various field distributions for the von Mises design and GTN design with $\bar{D} = 0.01$ are shown in Fig. 12. The results show that although more material is needed in the damage constrained designs with the GTN model, they have more uniformly distributed plastic work, better ductility (45.4% higher), higher load carrying capacity (29.0% higher), and higher plastic work dissipation (81.0% higher) before the failure occurs when compared to the von Mises design. The contributions of each damage mechanism in the GTN design are shown in Fig. 13, showing that the shear damage ($f_s = 0.3012$) is the dominating

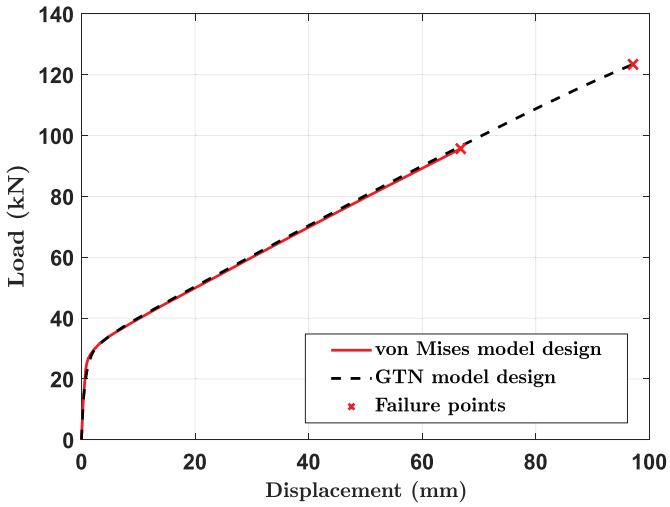

Fig. 14. Load-displacement curves for the optimized simply supported beam designs up to the failure points.

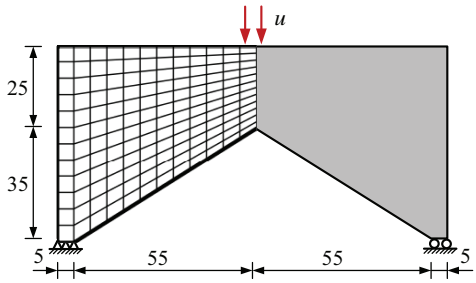

Fig. 15. Portal-frame design domain and finite element mesh (unit: mm).

failure mechanism in this design. The load-displacement curves for both the von Mises and GTN designs up to their failure points are shown in Fig. 14, again revealing the better performance of the GTN design.

Portal Frame—Mixed Stress Conditions

The third example concerns the design of a portal-frame type structure with a reentrant corner, as shown in Fig. 15. A downward displacement of $u = 10$ mm is applied along 5 mm in the middle of the top surface. Due to symmetry, only the left half of the domain discretized by 96×96 non-uniformly sized finite elements is optimized. The minimum plastic work to be dissipated is $\bar{W}^p = 205$ J, and the density filter radius is chosen as $r_{\min} = 1.5$ mm.

Again, the von Mises design with the optimized material volume fraction of $f_0 = 0.4973$ is first obtained as the reference design and is shown in Fig. 16(a). The plastic work, stress triaxiality, and effective damage distributions of this topology, when reanalyzed using the GTN model, are shown in Figs. 16(b–d), respectively. As shown in Fig. 16(b), the plastic work in this von Mises design is concentrated at two locations: support region and reentrant corner. Fig. 16(c) shows that the reentrant corner has high positive stress triaxiality, while in the support region there is negative stress triaxiality. The combination of high plastic strains and favorable stress states eventually leads to high damage at these locations, as shown in Fig. 16(d). The ultimate damage contribution plots shown in Fig. 17 reveal that the damage at the reentrant corner is dominated by the void growth (f_g), whereas damage in support regions is dominated by the void nucleation (f_N). The damage value of $f_1 = 0.2813$ at the reentrant corner and $f_2 = 0.0043$ at the support regions indicates that the void coalescence threshold ($f_c = 0.05$) has been exceeded at the reentrant corner in this von Mises design.

To mitigate the failure potential while still dissipating energy, the optimized design is obtained by considering the GTN model with $\bar{D} = 0.005$. The optimized design is shown in Fig. 18(a). In this design, more material ($f_0 = 0.5139$) is again required in order to satisfy the additional damage constraint. However, topological changes in this design enable a more uniformly distributed plastic work with decreased peak plastic work density, as shown in Fig. 18(b). Moreover, the high stresses in both positive triaxiality (reentrant corner) and negative triaxiality (support) locations have been relieved (from -1.10 to -0.91), as depicted in Fig. 18(c). Consequently, the maximum effective damage has been successfully constrained below $\bar{D} = 0.005$, i.e., $f^*_{\max} = 0.0047$.

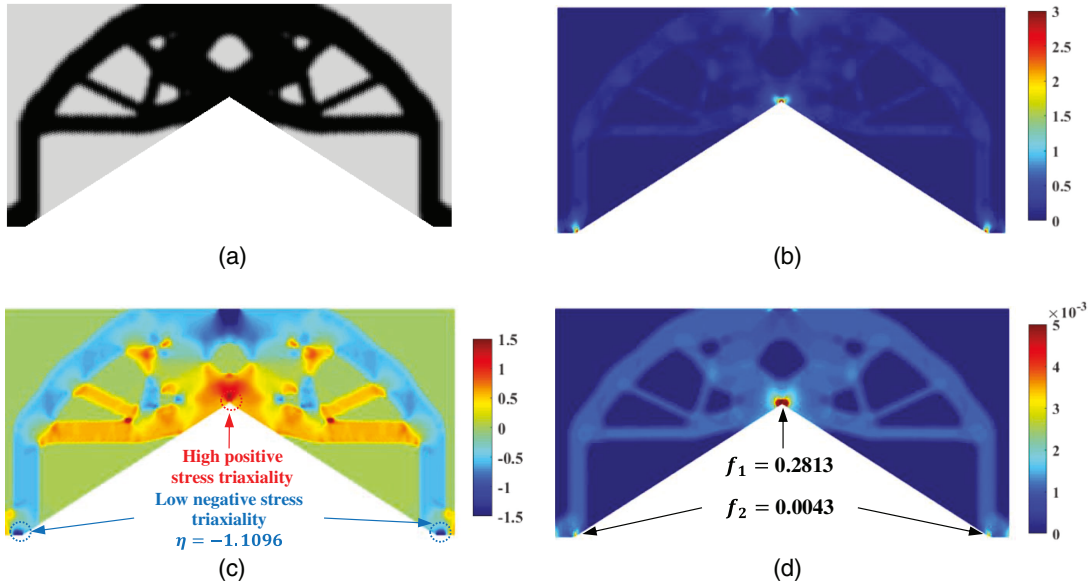

Fig. 16. Optimized portal-frame design using the von Mises model and the corresponding field distributions reanalyzed by the GTN model: (a) design, $f_0 = 0.4973$; (b) plastic work, $W^p = 204.47$ J; (c) stress triaxiality; and (d) effective damage, $f^*_{\max} = 0.6205$.

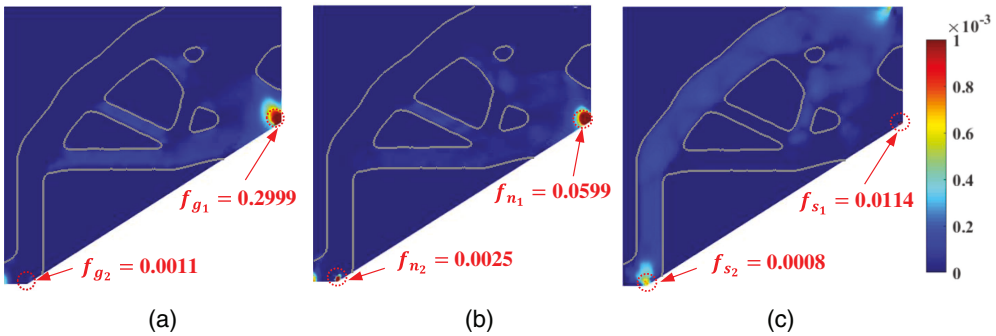

Fig. 17. Contributions of each damage mechanism for the von Mises portal-frame design at the failure point (scales are adjusted for a better visualization): (a) void growth f_g; (b) void nucleation f_n; and (c) void shear f_s.

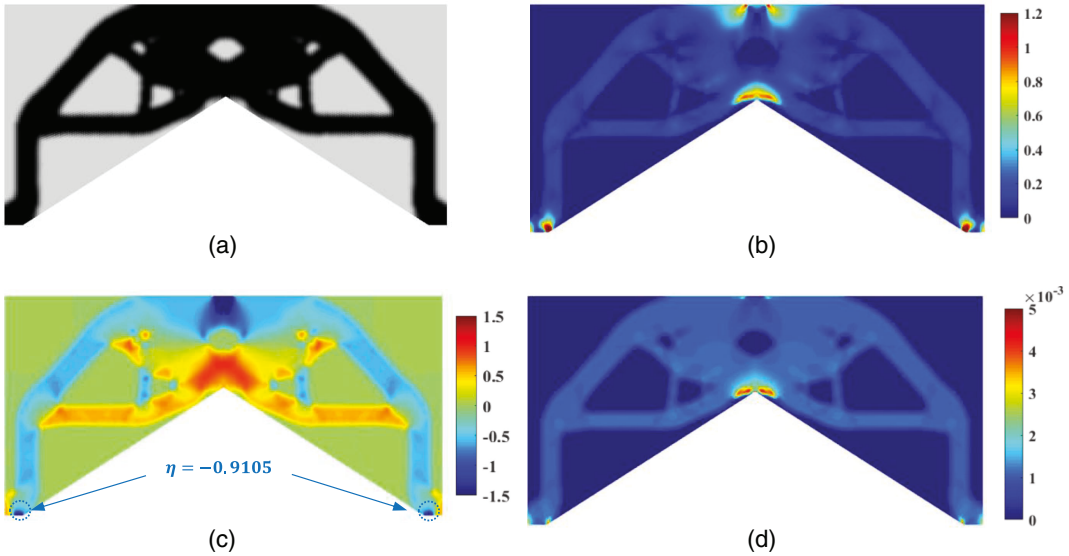

Fig. 18. Optimized portal-frame design using the GTN model with $\bar{D} = 0.005$ and the corresponding field distributions: (a) design, $f_0 = 0.5139$; (b) plastic work, $W^p = 205.00$ J.; (c) Stress triaxiality; and (d) effective damage, $f^*_{\max} = 0.0047$.

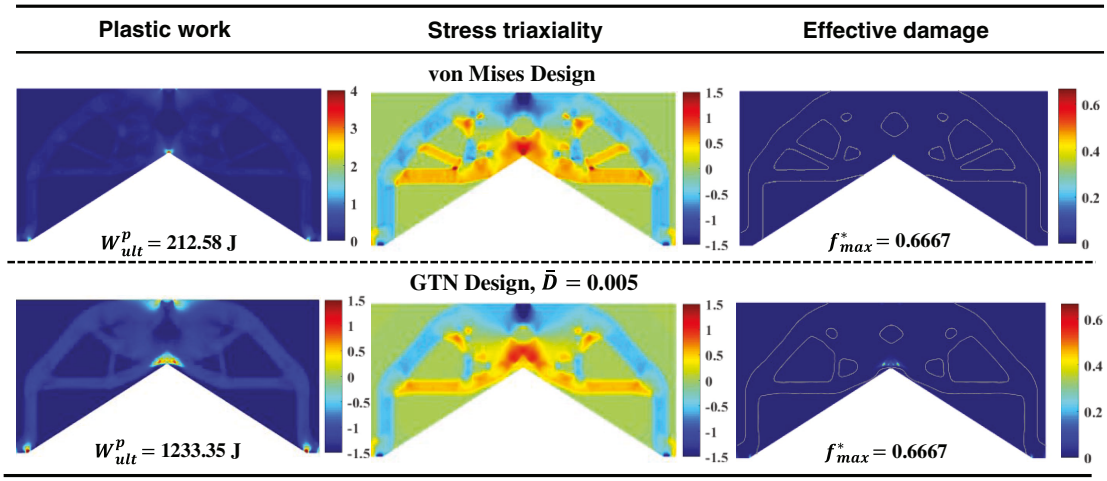

Fig. 19. Ultimate behaviors of the optimized portal-frame design with the GTN model at the failure point.

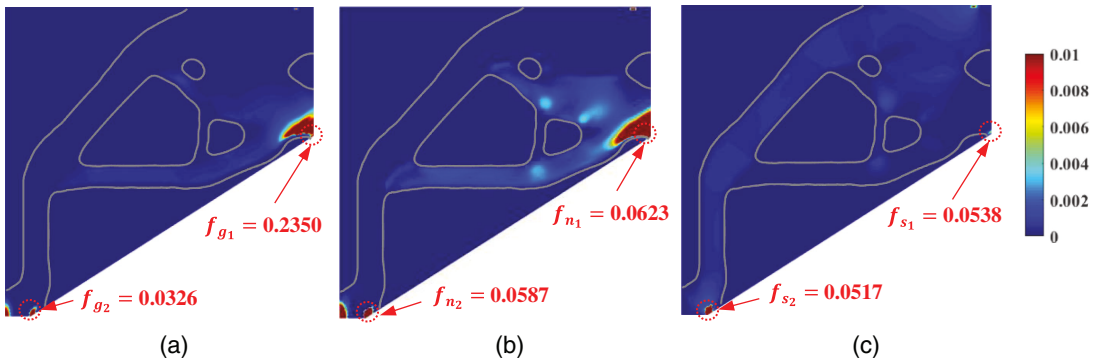

Fig. 20. Contributions of each damage mechanism for the GTN design at the failure point (scales are adjusted for a better visualization): (a) void growth f_g; (b) void nucleation f_n; and (c) void shear f_s.

Table 3. Performance comparison of the optimized portal-frame designs

Figure No.	Model	$\bar{D}$	Volume fraction	Ductility (mm)	Load carrying capacity (kN)	W^p_{ult} (J)
Fig. 16(a)	von Mises	N/A	0.4973	10.14	26.86	212.58
Fig. 18(a)	GTN	0.005	0.5139	36.81	51.14	1,233.35

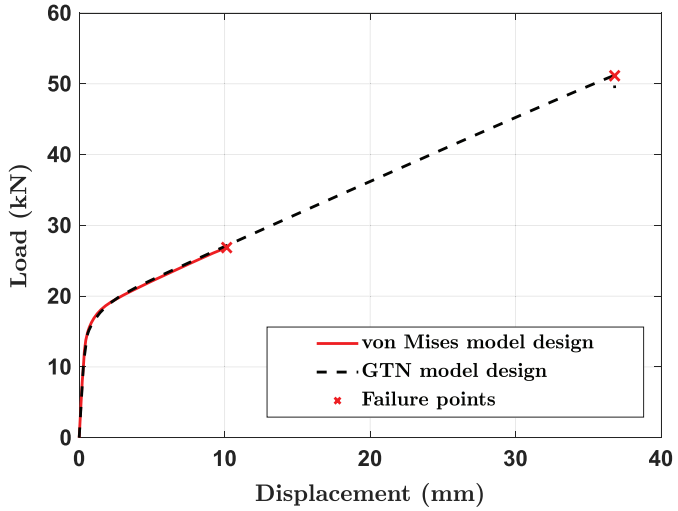

Fig. 21. Load-displacement curves for the optimized portal-frame designs up to the failure points.

Fig. 19 shows the field distributions of the von Mises and GTN designs at their failure points. It can again be observed that the plastic work is more evenly distributed in the GTN design (second row of Fig. 19) when compared to the von Mises design (first row of Fig. 19). The final failure initiates at the reentrant corner in both cases and is finally dominated by void growth under positive stress triaxiality. The damage mechanism plots for GTN design at its failure point shown in Fig. 20 reveal that the void growth ($f_{g_1} = 0.2350$) at the reentrant corner again governs the failure in this design. The ultimate performance comparison shown in Table 3 and the load-displacement curves depicted in Fig. 21 show that compared to the von Mises design, the GTN designs with damage constraints have much better performance in terms of ductility, load carrying capacity, and ultimate energy dissipation capacity. More importantly, this improvement in performance comes at the cost of only a small increase in the required material volume.

Conclusions

This study presents a design framework for failure resistant energy-dissipating plastic structures using density-based topology optimization. The micromechanically motivated Gurson–Tvergaard–Needleman (GTN) model with shear damage modifications is adopted to model the ductile damage mechanisms in metals. Appropriate design parametrization, scaling, and relaxation schemes are proposed to interpolate the corresponding material properties for intermediate-density elements to ensure numerical stability during the optimization process. Consistent and accurate path-dependent design sensitivities are obtained using the adjoint method for design variables update with a gradient-based optimizer. The effectiveness of the proposed design approach is demonstrated through selected numerical examples dominated by different failure mechanisms. The results show that the proposed optimization framework can limit the maximum damage in the optimized designs within the prescribed thresholds while simultaneously considering the physics of various damage mechanisms in a coupled manner. The results show that compared to the designs generated by the von Mises model, the failure resistant designs with the GTN model have overall better ductility, higher load carrying, and higher plastic energy dissipation capacities at the onset of failure. The tradeoff is a little more material usage in the GTN designs. This study represents the first effort to consistently incorporate the physics of ductile-damage mechanisms in topology optimization toward the design of energy-dissipating plastic structures. A natural extension of this work is to extend this framework to consider plasticity and damage under finite deformations and cyclic loading scenarios. However, this will require novel techniques to handle challenges associated with finite deformations (Zhang et al. 2018), and this will be addressed in our future work.

Data Availability Statement

All data, models, and code generated or used during the study appear in the published article.

Acknowledgments

The present work was supported in part by the US National Science Foundation through Grant No. CMMI-1762277. Any opinions, findings, conclusions, and recommendations expressed in this paper are those of the authors and do not necessarily reflect the views of the sponsors.

Supplemental Materials

All Supplemental Materials are available online in the ASCE Library (www.ascelibrary.org).

References

Alberdi, R., and K. Khandelwal. 2017. "Topology optimization of pressure dependent elastoplastic energy absorbing structures with material damage constraints." *Finite Elem. Anal. Des.* 133 (Oct): 42–61. https://doi.org/10.1016/j.finel.2017.05.004.

Alberdi, R., G. Zhang, L. Li, and K. Khandelwal. 2018. "A unified framework for nonlinear path-dependent sensitivity analysis in topology optimization." *Int. J. Numer. Methods Eng.* 115 (1): 1–56. https://doi.org/10.1002/nme.5794.

Anderson, T. L. 2017. *Fracture mechanics: Fundamentals and applications*. Boca Raton, FL: CRC Press.

Bao, Y., and T. Wierzbicki. 2004. "On fracture locus in the equivalent strain and stress triaxiality space." *Int. J. Mech. Sci.* 46 (1): 81–98. https://doi.org/10.1016/j.ijmecsci.2004.02.006.

Barsoum, I., and J. Faleskog. 2007. "Rupture mechanisms in combined tension and shear—Micromechanics." *Int. J. Solids Struct.* 44 (17): 5481–5498. https://doi.org/10.1016/j.ijsolstr.2007.01.010.

Beghini, L. L., A. Beghini, F. Baker William, and H. Paulino Glaucio. 2015. "Integrated discrete/continuum topology optimization framework for stiffness or global stability of high-rise buildings." *J. Struct. Eng.* 141 (8): 04014207. https://doi.org/10.1061/(ASCE)ST.1943-541X.0001164.

Bendsøe, M. P., and N. Kikuchi. 1988. "Generating optimal topologies in structural design using a homogenization method." *Comput. Methods Appl. Mech. Eng.* 71 (2): 197–224. https://doi.org/10.1016/0045-7825(88)90086-2.

Bendsøe, M. P., and O. Sigmund. 2003. *Topology optimization: Theory, methods and applications*. Berlin: Springer.

Bendsøe, P. M., and O. Sigmund. 1999. "Material interpolation schemes in topology optimization." *Arch. Appl. Mech.* 69 (9): 635–654. https://doi.org/10.1007/s004190050248.

Benzerga, A. A., and J.-B. Leblond. 2010. "Ductile fracture by void growth to coalescence." In *Advances in applied mechanics*, edited by H. Aref and E. V. D. Giessen, 169–305. Amsterdam, Netherlands: Elsevier.

Benzerga, A. A., J.-B. Leblond, A. Needleman, and V. Tvergaard. 2016. "Ductile failure modeling." *Int. J. Fract.* 201 (1): 29–80. https://doi.org/10.1007/s10704-016-0142-6.

Bourdin, B. 2001. "Filters in topology optimization." *Int. J. Numer. Methods Eng.* 50 (9): 2143–2158. https://doi.org/10.1002/nme.116.

Bruns, T. E., and D. A. Tortorelli. 2001. "Topology optimization of nonlinear elastic structures and compliant mechanisms." *Comput. Methods Appl. Mech. Eng.* 190 (26): 3443–3459. https://doi.org/10.1016/S0045-7825(00)00278-4.

Changizi, N., and M. Jalalpour. 2017. "Stress-based topology optimization of steel-frame structures using members with standard cross sections: Gradient-based approach." *J. Struct. Eng.* 143 (8): 04017078. https://doi.org/10.1061/(ASCE)ST.1943-541X.0001807.

Christensen, P. W., and A. Klarbring. 2008. *An introduction to structural optimization*. Dordrecht, Netherlands: Springer.

Chu, C. C., and A. Needleman. 1980. "Void nucleation effects in biaxially stretched sheets." *J. Eng. Mater. Technol.* 102 (3): 249–256. https://doi.org/10.1115/1.3224807.

Deaton, J. D., and R. V. Grandhi. 2014. "A survey of structural and multidisciplinary continuum topology optimization: Post 2000." *Struct. Multidiscip. Optim.* 49 (1): 1–38. https://doi.org/10.1007/s00158-013-0956-z.

de Souza Neto, E. A., D. Peric, and D. R. J. Owen. 2011. *Computational methods for plasticity: Theory and applications*. West Sussex, UK: Wiley.

El-Tawil, S., H. Li, and S. Kunnath. 2014. "Computational simulation of gravity-induced progressive collapse of steel-frame buildings: Current trends and future research needs." *J. Struct. Eng.* 140 (8): A2513001. https://doi.org/10.1061/(ASCE)ST.1943-541X.0000897.

Galjaard, S., S. Hofman, N. Perry, and S. Ren. 2015. "Optimizing structural building elements in metal by using additive manufacturing." In *Proc., IASS Annual Symposia*, 1–12. Amsterdam, Netherlands: International Association for Shell and Spatial Structures.

Garrison, W. M., and N. R. Moody. 1987. "Ductile fracture." *J. Phys. Chem. Solids* 48 (11): 1035–1074. https://doi.org/10.1016/0022-3697(87)90118-1.

Gibson, I., D. W. Rosen, and B. Stucker. 2014. *Additive manufacturing technologies*. New York: Springer.

Gurson, A. L. 1977. "Continuum theory of ductile rupture by void nucleation and growth: Part I—Yield criteria and flow rules for porous ductile media." *J. Eng. Mater. Technol.* 99 (1): 2–15. https://doi.org/10.1115/1.3443401.

Jewett, J. L., and J. V. Carstensen. 2019. "Experimental investigation of strut-and-tie layouts in deep RC beams designed with hybrid bi-linear topology optimization." *Eng. Struct.* 197 (Oct): 109322. https://doi.org/10.1016/j.engstruct.2019.109322.

Khandelwal, K., and S. El-Tawil. 2007. "Collapse behavior of steel special moment resisting frame connections." *J. Struct. Eng.* 133 (5): 646–655. https://doi.org/10.1061/(ASCE)0733-9445(2007)133:5(646).

Kiran, R., and K. Khandelwal. 2014. "Gurson model parameters for ductile fracture simulation in ASTM A992 steels." *Fatigue Fract. Eng. Mater. Struct.* 37 (2): 171–183. https://doi.org/10.1111/ffe.12097.

Lee, S., and A. Tovar. 2014. "Outrigger placement in tall buildings using topology optimization." *Eng. Struct.* 74 (Sep): 122–129. https://doi.org/10.1016/j.engstruct.2014.05.019.

Li, L., G. Zhang, and K. Khandelwal. 2017. "Topology optimization of energy absorbing structures with maximum damage constraint." *Int. J. Numer. Methods Eng.* 112 (7): 737–775. https://doi.org/10.1002/nme.5531.

Li, L., G. Zhang, and K. Khandelwal. 2018. "Failure resistant topology optimization of structures using nonlocal elastoplastic-damage model." *Struct. Multidiscip. Optim.* 58 (4): 1589–1618. https://doi.org/10.1007/s00158-018-1984-5.

Liang, Q. Q., B. Uy, and G. P. Steven. 2002. "Performance-based optimization for strut-tie modeling of structural concrete." *J. Struct. Eng.* 128 (6): 815–823. https://doi.org/10.1061/(ASCE)0733-9445(2002)128:6(815).

Liu, J., et al. 2018. "Current and future trends in topology optimization for additive manufacturing." *Struct. Multidiscip. Optim.* 57 (6): 2457–2483. https://doi.org/10.1007/s00158-018-1994-3.

Mijar, A. R., C. C. Swan, J. S. Arora, and I. Kosaka. 1998. "Continuum topology optimization for concept design of frame bracing systems." *J. Struct. Eng.* 124 (5): 541–550. https://doi.org/10.1061/(ASCE)0733-9445(1998)124:5(541).

Nabaki, K., J. Shen, and X. Huang. 2019. "Stress minimization of structures based on bidirectional evolutionary procedure." *J. Struct. Eng.* 145 (2): 04018256. https://doi.org/10.1061/(ASCE)ST.1943-541X.0002264.

Nahshon, K., and J. W. Hutchinson. 2008. "Modification of the Gurson model for shear failure." *Eur. J. Mech. A Solids* 27 (1): 1–17. https://doi.org/10.1016/j.euromechsol.2007.08.002.

Nielsen, K. L., and V. Tvergaard. 2010. "Ductile shear failure or plug failure of spot welds modelled by modified Gurson model." *Eng. Fract. Mech.* 77 (7): 1031–1047. https://doi.org/10.1016/j.engfracmech.2010.02.031.

Qian, X. D., Y. S. Choo, J. Y. Liew, and J. Wardenier. 2005. "Simulation of ductile fracture of circular hollow section joints using the Gurson model." *J. Struct. Eng.* 131 (5): 768–780. https://doi.org/10.1061/(ASCE)0733-9445(2005)131:5(768).

Rahmatalla, S., and C. C. Swan. 2003. "Form finding of sparse structures with continuum topology optimization." *J. Struct. Eng.* 129 (12): 1707–1716. https://doi.org/10.1061/(ASCE)0733-9445(2003)129:12(1707).

Sigmund, O., and K. Maute. 2013. "Topology optimization approaches." *Struct. Multidiscip. Optim.* 48 (6): 1031–1055. https://doi.org/10.1007/s00158-013-0978-6.

Svanberg, K. 1987. "The method of moving asymptotes—A new method for structural optimization." *Int. J. Numer. Methods Eng.* 24 (2): 359–373. https://doi.org/10.1002/nme.1620240207.

Tvergaard, V. 1982. "On localization in ductile materials containing spherical voids." *Int. J. Fract.* 18 (4): 237–252. https://doi.org/10.1007/bf00015686.

Tvergaard, V. 1989. "Material failure by void growth to coalescence." In *Advances in applied mechanics*, edited by J. W. Hutchinson and T. Y. Wu, 83–151. Amsterdam, Netherlands: Elsevier.

Tvergaard, V., and A. Needleman. 1984. "Analysis of the cup-cone fracture in a round tensile bar." *Acta Metall.* 32 (1): 157–169. https://doi.org/10.1016/0001-6160(84)90213-X.

Zhang, G., R. Alberdi, and K. Khandelwal. 2018. "Topology optimization with incompressible materials under small and finite deformations using mixed u/p elements." *Int. J. Numer. Methods Eng.* 115 (8): 1015–1052. https://doi.org/10.1002/nme.5834.

Zhang, G., L. Li, and K. Khandelwal. 2016a. "Topology optimization of structures with anisotropic plastic materials using enhanced assumed strain elements." *Struct. Multidiscip. Optim.* 55 (6): 1965–1988. https://doi.org/10.1007/s00158-016-1612-1.

Zhang, X., S. Maheshwari, A. S. Ramos, and G. H. Paulino. 2016b. "Macroelement and macropatch approaches to structural topology optimization using the ground structure method." *J. Struct. Eng.* 142 (11): 04016090. https://doi.org/10.1061/(ASCE)ST.1943-541X.0001524.

Zuo, Z. H., Y. M. Xie, and X. Huang. 2011. "Optimal topological design of periodic structures for natural frequencies." *J. Struct. Eng.* 137 (10): 1229–1240. https://doi.org/10.1061/(ASCE)ST.1943-541X.0000347.